

Powder Aerosol Deposition as a Method to Produce Garnet-Type Solid Ceramic Electrolytes: A Study on Electrochemical Film Properties and Industrial Applications

Tobias Nazarenus,* Yanyan Sun, Jörg Exner, Jaroslaw Kita, and Ralf Moos

Cyclable lithium batteries with a lithium metal anode are of great interest for future mobile and stationary applications due to their high potential energy density. To suppress lithium dendrite formation and growth, solid electrolytes (all-solid-state-batteries) are an alternative for liquid electrolytes. Compared with all other solid electrolytes, the ceramic lithium garnet solid electrolyte $\text{Li}_7\text{La}_3\text{Zr}_2\text{O}_{12}$ (LLZO) features a high thermal, electrochemical, and chemical stability. Due to its nonflammable nature, it is beneficial for battery cell safety. Despite major research efforts, an industrially applicable process route to produce the ceramic solid electrolyte has not been identified yet. Herein, film fabrication at room temperature of $\text{Al}_{0.2}\text{Li}_{6.025}\text{La}_3\text{Zr}_{1.625}\text{Ta}_{0.375}\text{O}_{12}$ (ALLZTO) via powder aerosol deposition (PAD) on a scalable apparatus is investigated. In addition to the description of synthesis and process conditions regarding industrial scalability, the sprayed 30 μm -thick PAD films are examined optically and electrochemically in half cells and symmetrical cells with lithium metal electrodes. By categorizing the process data and the electrochemical results compared with common reported production methods, a statement about the suitability for the industrial production of ceramic solid electrolytes using PAD is provided.

1. Introduction

Lithium metal batteries with solid-state electrolytes (SSEs) are promising as electrochemical storage devices for future stationary or mobile applications due to their potentially high specific energy density and increased safety compared with lithium-ion batteries with a liquid electrolyte.^[1,2] Different types of polymer

and ceramic solid electrolytes have recently been investigated regarding their chemical and electrochemical stability as well as their temperature-dependent ionic conductivity and processability.^[3,4] One of the most promising ceramic electrolytes to meet all these requirements is $\text{Li}_7\text{La}_3\text{Zr}_2\text{O}_{12}$ (LLZO) in the cubic garnet crystal structure. It shows a high thermodynamic and kinetic electrochemical stability to lithium metal electrodes,^[5,6] combined with a high ionic transfer number close to 1 and a high ionic conductivity of up to $10^{-3} \text{ S cm}^{-1}$ at room temperature that makes it favorable over other electrolytes.^[6] Usually, the cubic phase is stabilized by doping with Al^{3+} or/and Ta^{5+} . This also increases the conductivity and reduces the necessary sintering temperatures, yet also leads to a wide variety in reported compositions of $\text{Al}_y\text{Li}_{7-3y-z}\text{La}_3\text{Zr}_{2-z}\text{Ta}_z\text{O}_{12}$.^[7,8]

Although the production of sintered bulk samples produced by solid-state reaction with a high electrolyte thickness of several hundred micrometers allows remarkable current densities of up to 6 mA cm^{-2} at 60°C with high solid electrolyte conductivities of up to $10^{-3} \text{ S cm}^{-1}$ at room temperature, a commercial industrial large-scale production with high throughput rates in combination with moisture-free processing is challenging.^[9–11] Ideally, the thickness of the electrolyte should be in the range of 5–20 μm to reduce the risk of short circuits on the one hand but, on the other hand, provide a low electrolyte mass for high cell energy densities.^[12] Although much research has been conducted, the thickness range for LLZO films significantly below 50 μm could only rarely be realized yet due to the non-availability of suitable ceramic production technologies.^[13] Sintering of tape-casted ceramic electrolytes is an often reported method to produce tapes below 0.5 mm.^[14–24] However, high sintering temperatures $>1000^\circ\text{C}$ in combination with dwell times of several hours lead to high investment and operating costs. Furthermore, an exact temperature control is necessary to achieve thin planar ceramic plates without deformation.^[25–27] Alternative fabrication methods like metal organic chemical vapor deposition (MO-CVD),^[28,29] pulsed laser deposition (PLD),^[17,30–38] radio frequency (RF) sputtering,^[39–45] and atomic layer deposition (ALD)^[46] have been investigated to produce films in a nanometer scale. However, all these coating techniques

T. Nazarenus, Prof. R. Moos
Bavarian Center for Battery Technology (BayBatt)
Universitätsstr. 30, 95447 Bayreuth, Germany
E-mail: Functional.Materials@uni-bayreuth.de

T. Nazarenus, Y. Sun, Dr. J. Exner, Dr. J. Kita, Prof. R. Moos
Department of Functional Materials
University of Bayreuth
Universitätsstraße 30, 95447 Bayreuth, Germany

 The ORCID identification number(s) for the author(s) of this article can be found under <https://doi.org/10.1002/ente.202100211>.

© 2021 The Authors. Energy Technology published by Wiley-VCH GmbH. This is an open access article under the terms of the Creative Commons Attribution License, which permits use, distribution and reproduction in any medium, provided the original work is properly cited.

DOI: 10.1002/ente.202100211

usually require temperatures above 500 °C to obtain a sufficient ionic conductivity of the ceramic solid electrolytes. Furthermore, only few electrolytes with a film thickness below 50 µm and processing temperatures <1000 °C have yet been cycled with lithium metal electrode.

The powder aerosol deposition (abbreviated as PAD, also known as aerosol deposition, vacuum cold spray, or vacuum kinetic spray) method in contrast allows to fabricate well-adhering films directly with an inexpensive process infrastructure at room temperature without the risk of interdiffusion reactions or mechanical failure due to different thermal expansion coefficients of the SSE with possible electrode materials. In addition, PAD is characterized by the highest deposition rates of 1–2 µm min⁻¹ compared with other coating methods like MO-CVD, PLD, RF sputtering, or ALD, and high coating areas with a reported width of up to 40 cm.^[47,48] Thus, a high sample throughput is possible in a future cell production. However, the technology readiness level (TRL) 4 has to be achieved to be relevant for an industrial application.^[49]

Even though the LLZO solid electrolyte appears to be stable versus a lithium metal electrode, the interface between the two components is an often-addressed topic in literature.^[50–52] A major reported challenge is the lithiophobic character of the LLZO surface, which is often caused by degradation mechanisms in humid atmosphere. To meet this challenge, two different strategies have been investigated: on one hand, the surface is polished to remove possible reaction products and get a homogeneous, plane surface where the lithium electrode is pressed on.^[51,53] On the other hand, various interlayers are introduced to increase the wettability and therefore the total contact area or decrease the interface resistance.^[54–56]

In this work, we synthesized Al_{0.2}Li_{6.025}La₃Zr_{1.625}Ta_{0.375}O₁₂ (ALLZTO) solid electrolyte powder by a mixed-oxide route and prepared 30 µm-thick films by the powder aerosol deposition method (PADM). To increase the film conductivity and to enable a stable electrochemical cycling of symmetrical Li|ALLZTO|Li cells, two cell modifications have additionally been investigated: a thermal post-treatment was conducted at 400 °C in nitrogen atmosphere, and a graphite interlayer was applied. Films were characterized by electrochemical and optical measurements. As PAD is a promising technique to produce ceramic electrolytes for future lithium metal batteries, we describe the deposition method in detail and also provide technical process data to compare the fabrication method to competing methods.

2. Experimental Section

2.1. Powder Synthesis

ALLZTO garnet-type powder was synthesized via the mixed-oxide route. The composition is reported to show a high stability and conductivity.^[7,57,58] The precursor powders of α-Al₂O₃ (ALMATIS), La₂O₃ (Alfa Aesar, 99.9%), Ta₂O₅ (Alfa Aesar, 99.5%), and ZrO₂ (99.5%) were dried at 120 °C for 24 h as well as Li₂CO₃ powder (Alfa Aesar, 99%) at 1000 °C in alumina crucibles for 10 h to obtain moisture-free powders. The dried powders were weighed in stoichiometrically with 10 wt% excess of

Li₂CO₃ and ball milled in a planetary ball mill (Fritsch Pulverisette 5, Idar-Oberstein). The powders were homogenization milled in deionized water as a milling fluid in zirconia milling jars (ZrO₂, stabilized with 3.5 wt% MgO) with zirconia balls (ø2 mm, ZrO₂, stabilized with 5 mol% Y₂O₃) at 400 rpm for 9 min. After drying in a rotary evaporator (Heidolph Hei-VAP Advantage, Schwabach, Germany), the powder mixture was calcined at 1000 °C in an alumina crucible for 6 h, with a heating and cooling rate of 5 K min⁻¹. During cooling when reaching a temperature of 350 °C, the calcined powders were transferred into a nitrogen glovebox (GS Glovebox Systemtechnik GmbH, Germany) with a dew point (*T*_{dp}) below -50 °C. To obtain micrometer-sized particles, the synthesized powder was ground again by dry milling in nitrogen atmosphere with zirconia balls (ø10 mm, ZrO₂, stabilized with 5 mol% Y₂O₃) at 120 rpm for 1 h and at 100 rpm for 1 h. After sieving, the powder (mesh size 56 µm) to remove large agglomerates, the powder was stored in an argon filled glovebox (*T*_{dp} < -80 °C) until it was used to fabricate films by PADM.

2.2. Film Fabrication and Half-Cell Assembly

A custom-built PAD apparatus was used to fabricate thin-solid electrolyte films in nitrogen atmosphere according to the process sequence in **Figure 1**. Compared with the classical PAD setup as described in literature, it was modified to meet additional requirements for processing LLZO powder into layers.^[59–62] To enable the continuous coating over long coating times in an inert atmosphere, the aerosol generation was implemented in a glovebox with a large powder reservoir. A venturi nozzle allowed the exact adjustment of the aerosol concentration. For film fabrication, a nitrogen carrier gas flow of 8 L min⁻¹ and an oxygen dispersing gas flow of 4 L min⁻¹ were chosen. This resulted in an aerosol jet with a calculated aerosol concentration of 110 mg L⁻¹ that entered the nozzle. By the used slit nozzle with an orifice of 25 × 0.4 mm², the aerosol is accelerated toward the polished copper substrates in 3 mm distance. The surfaces of the 1 mm-thick copper substrates were polished with sandpaper (1200 grit SiC, 5 µm grain size) before the PAD process to obtain a plane surface with low roughness for the electrochemical analysis after the cell assembly. Then they were placed on the substrate holder. The substrates were horizontally moved with 1 mm s⁻¹ by the programmable *x*-*y* platform to enable coating areas of up to 25 × 25 mm². For the subsequent half-cell assembly, three different procedures were used:

First (type I), processing took place without further modifications. Lithium metal foils were directly placed on the polished solid electrolyte. Second (type II), samples were annealed in a furnace at 400 °C for 1 h with heating and cooling rates of 5 K min⁻¹ in nitrogen atmosphere with a constant gas flow of 1.25 L min⁻¹ before the lithium metal foil electrode was placed on the polished surface. By the thermal post-treatment, the atomic lattice deformation, which is caused by the deposition method, should be reduced.^[62] Third (type III), to increase the electronic conductive contact area between the solid electrolyte and the lithium electrode, an ≈1 µm graphite interlayer was manually applied with a graphite rod without a thermal post-treatment. Details can be obtained from

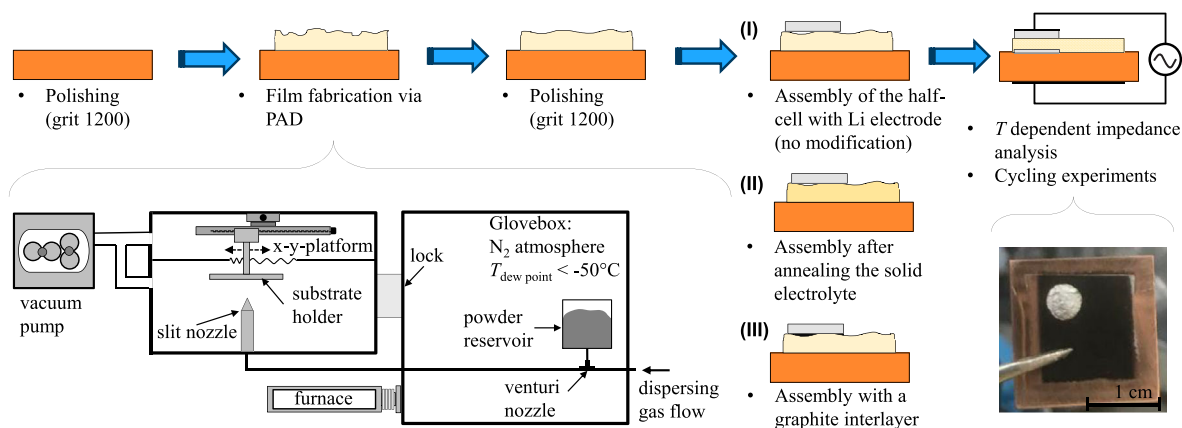


Figure 1. Experimental protocol for half-cell, respectively, symmetrical cell manufacturing of an ALLZTO film on copper substrates via PAD method with lithium metal foil electrode: (I) assembly of lithium foil on the solid electrolyte in the as-deposited state after polishing; (II) assembly of the solid electrolyte and the lithium metal electrode after thermal annealing at 400°C with and without a subsequent thermal treatment of the half-cell; (III) assembly of the solid electrolyte in the as-deposited state and the lithium metal electrode after polishing and applying a graphite interlayer; electrochemical analysis: temperature-dependent EIS and cycling at 70°C .

Figure S1, Supporting Information. Figure 1 shows the experimental protocol for the half-cell assembly after the film formation via PAD apparatus.

2.3. Powder, Film Fabrication, and Half-Cell Characterization

The powder was analyzed by X-ray diffractometry (D8 Advance, Bruker, USA) between 15° and 70° (2θ) in steps of 0.02° for a hold time of 1 s. The reflex pattern recorded with the diffractometer (Cu anode 2.2 kW, = nm, Ge $K\alpha 1$ monochromator, 1D-Lynxeye detector) were evaluated regarding their quantitative phase composition according to the Rietveld refinement method by the X'Pert HighScore Plus software. The particle size distribution was measured by Malvern Mastersizer 2000. Scanning electron microscopy (SEM) images of the powder as well as of the PAD films were obtained using a Zeiss Leo Gemini 1530 (inlens and secondary electron detector).

The deposition rate r during film fabrication was calculated according to Equation (1), with the film thickness t_s , the nozzle width b_D , the coating speed v_s , and the number of scans n_w .^[59]

$$r = \frac{t_s}{n_w} \times b_D \times v_s \quad (1)$$

After the deposition of the powder on copper substrates, the samples were directly transferred into the attached glovebox so that the samples were not exposed to moisture atmosphere and subsequently polished with sandpaper (1200 grit, SiC, $5\ \mu\text{m}$ grain size) to flatten the surface and to remove isolating surface layers.^[53,63] The film thickness and roughness of the ceramic electrolyte was determined by the profile stylus instrument-type Jenoptik Waveline W20. The half-cell with a lithium metal electrode ($\varnothing 5\ \text{mm}$, $0.75\ \text{mm}$ thickness) was assembled in a separate argon-filled glovebox ($T_{\text{dp}} < -80^\circ\text{C}$). In the cell assembly without modifications, the $30\ \mu\text{m}$ -thick solid electrolyte was contacted with a lithium metal anode directly after polishing. The lithium electrode was manually pressed onto the solid electrolyte. Neither

a temperature treatment nor a surface modification except polishing was conducted. The graphite layer was applied manually by a graphite pencil according to literature.^[56]

All cells were measured by electrochemical impedance spectroscopy (EIS, Zahner Zennium, $f = 1\ \text{MHz}$ to $1\ \text{Hz}$, sinusoidal signal amplitude $U_{\text{rms}} = 25\ \text{mV}$) during heating from room temperature to 70°C in the argon glovebox ($T_{\text{dp}} < -80^\circ\text{C}$) in the measurement setup shown in Figure S2, Supporting Information. The effective conductivity σ_{eff} is calculated according to Equation (2) with contact area A , the measured resistance R as difference between the intersections of the semicircle with the real axis in the Nyquist plot and the film thickness t_s .^[64]

$$\sigma_{\text{eff}} = \frac{t_s}{R \times A} \quad (2)$$

By calculating the slope in the Arrhenius representation, the activation energy E_A was determined from Equation (3) using the absolute temperature T , the Boltzmann constant k_B , the effective conductivity σ_{eff} and pre-exponential factor B .^[64]

$$\sigma_{\text{eff}} = \frac{B}{T} e^{\left(-\frac{E_A}{k_B T}\right)} \quad (3)$$

The ionic conductivity σ_{ion} depends on the elementary charge e , the density of available ionic charge carriers n and their mobility μ and is calculated according to Equation (4).^[64]

$$\sigma_{\text{ion}} = e \times n \times \mu \quad (4)$$

At $\approx 70^\circ\text{C}$, lithium ions were forced through the ALLZTO electrolyte to the ALLZTO|Cu interface during cycling by applying a constant current with a current density of ± 15 and $\pm 30\ \mu\text{A cm}^{-2}$ for 30 min from the top lithium electrode to the bottom copper electrode and 10 min vice versa. Equation (5) is used to calculate the lithium layer thickness that forms at the interface to the blocking copper electrode. The thickness depends on the applied current I , the Faraday constant F , the molar mass

of lithium M_{Li} , the charge number z , the theoretical density of lithium ρ_{Li} as well the time t the current was applied, and the contact area A .^[65]

$$d = \frac{M_{\text{Li}} \cdot I \cdot t}{z \cdot A \cdot \rho_{\text{Li}} \cdot F} \quad (5)$$

For each half cell, a calculated reservoir of at least 1 μm was plated before cycling. During the following cycling of the cells, the polarization duration in each direction remained constant for each chosen current density. The absolute polarization duration decreased with increasing current density, so that the Li reservoir thickness remained constant. At some points, significantly shorter cycling durations occurred due to deviations caused by the written program code within software used for the cycling experiments.

3. Results and Discussion

3.1. Powder Characterization

The $\text{Al}_{0.2}\text{Li}_{6.025}\text{La}_3\text{Zr}_{1.625}\text{Ta}_{0.375}\text{O}_{12}$ powder was synthesized in the cubic garnet type structure at 1000 °C, as shown in the X-ray diffraction (XRD) pattern in **Figure 2a**, with two secondary phases. The pattern of cubic LLZO (ICDD 04-018-9023) is added for comparison. The low amount of the secondary phases, namely $\text{La}_2\text{Zr}_2\text{O}_7$ (ICDD 00-017-0450) and LaAlO_3 (ICDD 04-007-2676), was determined by Rietveld refinement to be <1 wt% each. Although a relatively low amount of alumina is used for doping, an aluminum-rich phase (LaAlO_3) occurs in the XRD pattern. This may be caused by interdiffusion reactions during calcination in the alumina crucible at 1000 °C.

The high calcination temperature might also lead to lithium losses due to evaporation and therefore results in both observed secondary phases with no lithium content.

The dry-milled powder exhibits a bimodal particle size distribution with two maxima at 0.7 and 6 μm . Although the bimodal distribution of the particle size may negatively affect the deposition mechanism due to large particles with a high impact impulse, particles sizes with $D_{50} \approx 4.2 \mu\text{m}$ are in general suitable for PAD coating within the reported process window.^[59]

The SEM image in **Figure 2c** shows the particle size distribution. The powder mainly consists of irregular shaped, edged particles. A fine powder fraction (<200 nm) covers the surface of bigger primary particles ($\approx 8 \mu\text{m}$).

3.2. Film Formation via PAD

The powder is deposited on an area of $12 \times 12 \text{ mm}^2$ with a film thickness of 30 μm on copper substrates. The particle size distribution in combination with a constant, yet comparably low, aerosol concentration leads to a deposition rate of $\approx 0.1 \text{ mm}^3 \text{ min}^{-1}$ according to Equation (1). In addition, the deposition rate may be improved further by the nozzle geometry and the number of nozzles. The SEM image in **Figure 3a** also shows the typical impactation-derived structure of the surface with impact craters in the as-deposited state.

By polishing the surface after deposition, the roughness (characterized by the center line average roughness value R_a

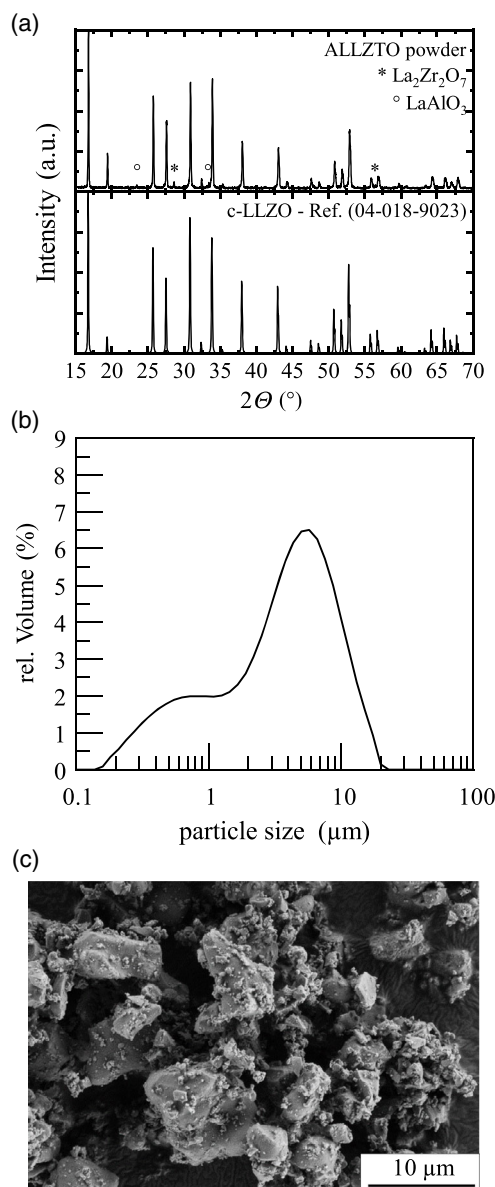


Figure 2. Characterization of the $\text{Al}_{0.2}\text{Li}_{6.025}\text{La}_3\text{Zr}_{1.625}\text{Ta}_{0.375}\text{O}_{12}$ powder: a) XRD pattern of the synthesized powder in comparison with cubic LLZO reference material (ICDD 04-018-9023). The secondary phases $\text{La}_2\text{Zr}_2\text{O}_7$ and LaAlO_3 are marked with an asterisk and a circle, respectively, b) bimodal particle size distribution of the powder after dry milling; c) SEM image of the ALLZTO powder after dry milling.

and the mean peak-to-valley height R_z) was significantly reduced from $R_a = 0.12 \mu\text{m}$ and $R_z = 0.65 \mu\text{m}$ in the as-deposited state to $R_a = 0.06 \mu\text{m}$ and $R_z = 0.45 \mu\text{m}$ after polishing, also visible when comparing **Figure 3a,b**. A low ratio of film roughness to film thickness is beneficial for a homogeneous electrical field distribution through the solid electrolyte and may therefore reduce to the lithium dendrite formation.^[66] Furthermore, polishing removes Li_2CO_3 surface layers that may form despite processing in dry glovebox atmospheres.^[53,67]

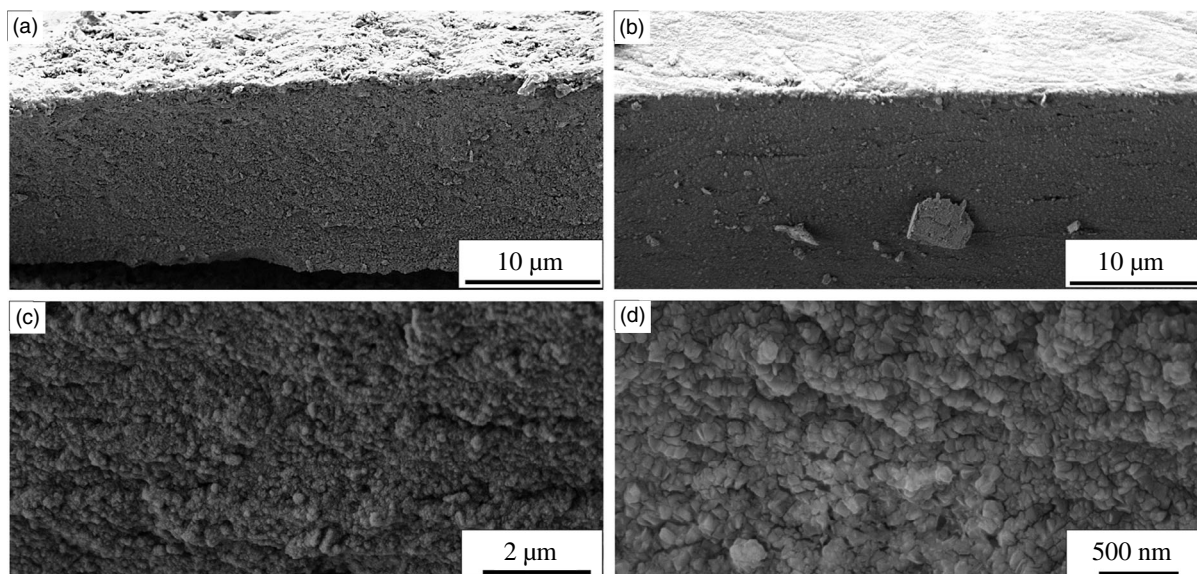


Figure 3. Fractured cross-sectional SEM images of the ALLZTO PAD film in a) the as-deposition state before and b–d) after polishing. c,d) Higher magnifications validate the dense and nanocrystalline structure of the films.

Figure 3c,d shows the microstructure of the dense and homogeneous film that is characterized by nanometer-sized grains. The initial micrometer-sized particles fracture according to the room temperature impact consolidation (RTIC) mechanism through grains and grain boundaries and form unsaturated surfaces as explained in detail in the following paragraph. Although the exact film formation mechanism has not yet been fully understood, the unsaturated surfaces may play an important role and result in well-adhering PAD films on a variety of substrates.^[59]

3.3. Cell Assembly without Modifications (Type I)

The temperature-dependent EIS measurements of the cell in the as-deposited state are shown in **Figure 4a**. As expected, the total resistances get reduced with increasing measuring temperatures. Although the EIS spectra contain at least four different contributions (ALLZTO|Li-interface, ALLZTO grain conductivity, ALLZTO grain boundary conductivity and the blocking Cu electrode), only single deflated semicircle is visible in the Nyquist plot. The mobility of the ionic charge carriers is reduced due

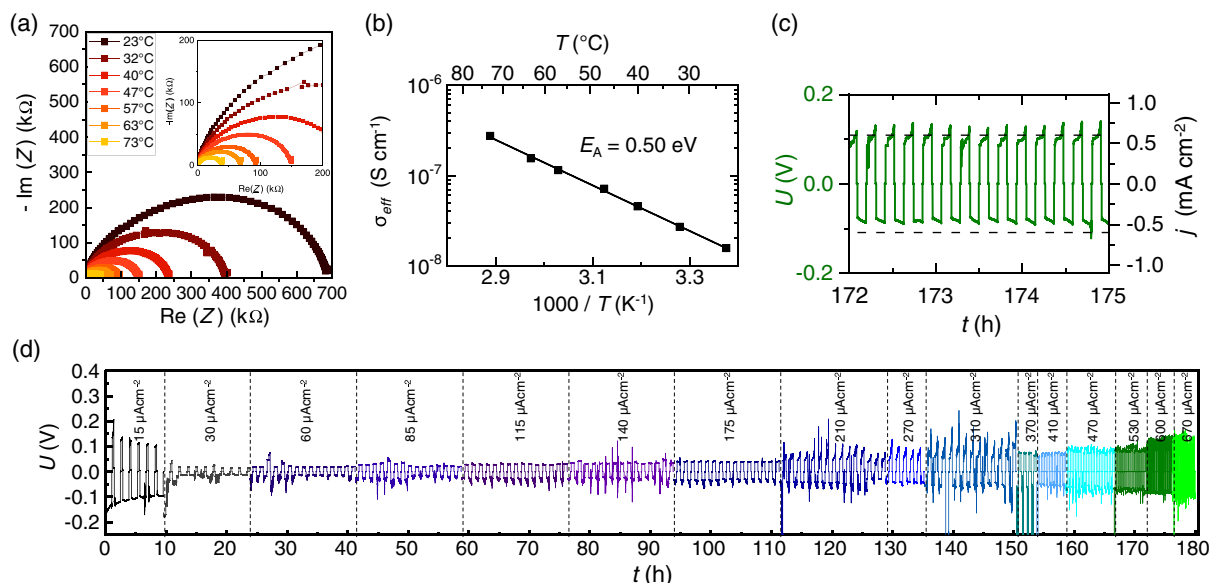


Figure 4. Electrochemical characterization of polished as-deposited ALLZTO films (type I): a) Nyquist plots of temperature-dependent EIS measurements, b) Arrhenius plot of the calculated effective conductivity values, c) partially extracted current–voltage relationship during cycling at $600 \mu\text{A cm}^{-2}$ from (d), d) complete cycling test at 70°C with a critical current density of $670 \mu\text{A cm}^{-2}$.

to the distorted atomic lattice of PAD films in the as-deposited state.^[68]

The high particle impact energy leads to a densification of the film but also causes a lattice deformation.^[69] At higher temperatures (>50 °C), a diffusion limitation contribution caused by the blocking copper electrode is visible due to the increased mobility of the lithium ions. The Arrhenius plot shows a linear relation between inverse temperature and logarithmic conductivity. At 23 °C, the effective through-plane conductivity of the sample in the as-deposited state is $1.6 \times 10^{-8} \text{ S cm}^{-1}$, which is four to five orders of magnitude lower than bulk materials.^[70] The measured through-plane conductivity is even one order of magnitude lower than the in-plane conductivity of ALLZTO films on platinum interdigitated electrodes.^[62] This phenomenon has already been described in literature and is explained by the particle lattice deformation as well as by the layered film structure with a slight anisotropy in the electrical properties.^[71] During the RTIC, the powder particles collide with the substrate and fracture through grain boundaries and grains. The ongoing particle bombardment leads to a densification of the film, also known as hammering effect, and results in a distorted atomic lattice.^[60,72] Consequently, the particles may be deformed, whereas the atomic lattice is vertically compressed in relation to the substrate orientation. Therefore, the in-plane conductivity can be higher because of a reduced amount of grain boundaries on the one hand and a higher horizontal ion mobility within the grain on the other hand. Furthermore, the measurement setup has been considered. The lithium application might not be ideal and therefore a low contact area may cause reduced effective conductivity values. Nevertheless, the result is in good agreement with previous results for LLZO films with a lithium metal electrode when fabricated by PAD.^[73,74] By increasing the temperature, the effective resistance decreases as well as the ionic conduction shifts to lower time constants. Therefore, the diffusion-blocking copper electrode becomes visible in the Nyquist plots at higher temperatures (>50 °C) and low frequencies. At 73 °C, a maximum effective conductivity of $2.8 \cdot 10^{-7} \text{ S cm}^{-1}$ is calculated. The resulting activation energy of 0.50 eV is also increased compared with 0.30–0.40 eV for sintered bulk samples in literature.^[75] We attribute the higher value to the microstructure and the distorted lattice of the film. Due to the nanometer-sized grains, charge carrier transport is governed by grain boundary resistances rather than by the internal bulk resistance, which is reportedly higher.^[51] In addition, the deformed lattice constants may decrease the mobility of the charge carriers and therefore increase the activation energy. Alternatively, the temperature-dependent resistance can also be dominated by the Li|ALLZTO interface, which may also be indicated by an increased activation energy. During cycling with 15 and $30 \mu\text{A cm}^{-2}$, a lithium reservoir with a thickness of 1.1 μm is formed at the interface between the ALLZTO and the copper substrate, according to Equation (5). As it is shown in Figure 4d, during polarization and cycling with lithium metal electrodes at 70 °C, short voltage peaks occur to keep a constant current. As the voltage depends on the parameters mentioned in Equation (2) and as the resistances of the solid electrolyte as well as the current are constant, the contact area is reduced during the voltage peaks. This behavior can be explained by the formation of gaps between the lithium electrode and the solid electrolyte.^[51]

Due to the remaining roughness in combination with a too low externally applied pressure onto the cell, contact losses during cycling can occur and the reduced solid–solid contact area leads to locally increased current densities.^[51] Furthermore, the voltage peaks primarily occur during negative polarization, respectively, during the plating of lithium between ALLZTO and copper. This phenomenon can be explained by the strong bonding between the ALLZTO film and the copper substrate after the deposition. Based on the cycling experiment, the electrochemically plated lithium between the solid electrolyte and the copper substrate shows a significantly reduced number of gaps between the solid electrolyte and the lithium metal. In Figure 4c, the cycling behavior with a current density of $600 \mu\text{A cm}^{-2}$ at 70 °C is shown. According to Equation (2), the effective DC conductivity is increased to $1.8 \times 10^{-5} \text{ S cm}^{-1}$ compared with $2.8 \times 10^{-7} \text{ S cm}^{-1}$ during initial heating. This fact can be caused at least by two reasons: On the one hand, undesired lithium dendrites are slowly forming and reduce the resistance and on the other hand, the interface area is increased. At 70 °C, the lithium might be sufficiently ductile to close initial gaps over time. This would also mean that the effective conductivity in Figure 4a shows dominated by the interface between the lithium metal electrode and the solid electrolyte, and the assumed contact area is incorrect due to gaps and therefore the real conductivity might be higher compared with the calculated values.

3.4. Cell Assembly of a Thermally Annealed Solid Electrolyte (Type II)

Hanft et al. reported the beneficial influence of a thermal post-treatment on the ion conductivity of ALLZTO films after deposition.^[62] More recently, a general relationship between the required annealing temperature and the coating material was found.^[68] The annealing temperature is chosen based on published results, that indicate a major reduction of lattice deformation and therefore increase in conductivity at that temperature.^[62] Regarding a future cell production of a cathode supported cell, annealing should be conducted at the lowest possible temperatures to prevent interdiffusion processes that are high enough for a sufficient increase in ionic conductivity. In Figure 5, the electrochemical behavior of samples annealed at 400 °C is shown. Already at 25 °C, the resistance of the annealed 30 μm -thick sample is significantly reduced compared with the as-deposited state as it is shown in the Nyquist and Arrhenius plots in Figure 5a,b, respectively.

The Nyquist plots show an offset that is caused by the measurement setup. At room temperature (25 °C), a conductivity of $4.7 \times 10^{-5} \text{ S cm}^{-1}$ is measured, which is more than three orders of magnitude higher than in the as-deposited state. At 70 °C, a maximum conductivity of $3.1 \times 10^{-4} \text{ S cm}^{-1}$ is reached. The permanent increase in the ionic conductivity after a thermal annealing at 400 °C is attributed to the microstrain reduction within the atomic lattice.^[62] A temperature of 400 °C is, however, insufficient for crystallite growth. The higher lattice order results in a higher ionic mobility and therefore a higher conductivity according to Equation (4). Due to the increased ionic mobility in the annealed sample, the blocking copper electrode can be detected in the Nyquist plot already at

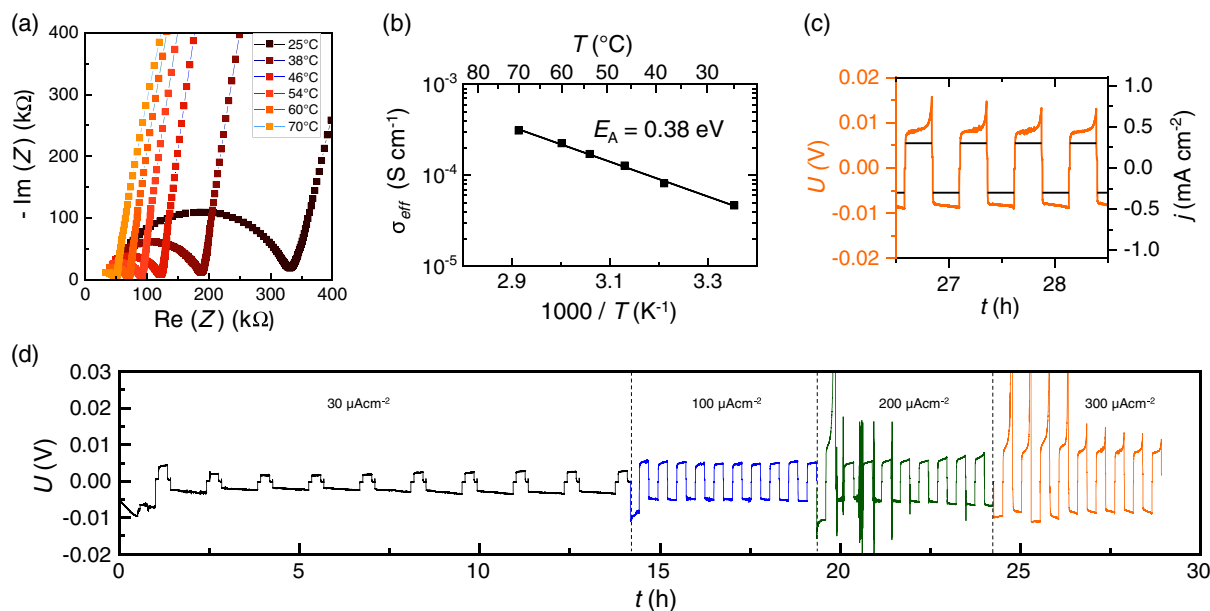


Figure 5. Electrochemical characterization of the polished and at 400 °C annealed ALLZTO film (type II): a) Nyquist plots of temperature-dependent EIS measurements, please note that compared with Figure 4 the scale of the axes is reduced by a factor of 1000, b) Arrhenius plot of the calculated conductivities, c) partially extracted current–voltage relationship during cycling at 300 $\mu\text{A cm}^{-2}$ from d), d) complete cycling test at 70 °C with a critical current density of 300 $\mu\text{A cm}^{-2}$.

room temperature, whereas it can be only detected for $T > 50\text{ }^{\circ}\text{C}$ in the as-deposited sample. Furthermore, thermal annealing leads to a lower activation energy (0.38 eV), as shown in Figure 5. This value is close to the reported activation energies for grain boundaries in LLZO sintered bulk materials in literature and indicates a homogeneous, undistorted crystalline lattice structure.^[51] The reduced electrical resistance leads to lower voltages during the cycling measurements, as shown in Figure 5d. During cycling with 30 $\mu\text{A cm}^{-2}$, a lithium reservoir of 1 μm thickness is formed according to Equation (5). The cycling of the PAD film with a current density of 0.1 mA cm^{-2} at 70 °C does not lead to contact losses and voltage peaks. At higher current densities, voltage peaks indicate contact losses of the electrolyte to the lithium electrode. Based on the measurement data in Figure 5c as well as Equation (2) and Ohms law, the conductivity during DC cycling can be determined to $9.0 \times 10^{-4}\text{ S cm}^{-1}$. This may again, as explained earlier, be caused by dendrite formation or by a high contact area without voids. This cell preparation allows a maximum current density of 300 $\mu\text{A cm}^{-2}$, which is lower compared with the polished sample in the as-deposited state. The earlier failure can be a result of the annealing process at 400 °C. Due to different thermal expansion coefficients of the ALLZTO film and the copper substrate, film cracks may occur causing a short circuit.^[62]

3.5. Cell Assembly with a Graphite Interlayer (Type III)

To increase the critical current density and improve the electrolyte–electrode interface, a graphite layer is applied onto the polished surface of a 30 μm -thick ALLZTO film. To reduce the risk of crack formation, the ALLZTO films are not thermally annealed. Figure 6 shows the Nyquist plots of the impedance

spectra during initial heating. The calculated temperature-dependent conductivity is shown in the Arrhenius plot in Figure 6b. Compared with the direct cell assembly in Figure 4, the conductivity is increased from $1.6 \times 10^{-8}\text{ S cm}^{-1}$ in the as-deposited state at 23 °C to $6.6 \times 10^{-8}\text{ S cm}^{-1}$ at 29 °C with a graphite interlayer. Due to the low ionic mobility, the blocking electrode is barely visible in the Nyquist plots as discussed previously. The increased conductivity can be caused by an increased surface contact area where the graphite fills the uneven surface gaps between the solid electrolyte and the lithium electrode. In this case, the electronically conductive graphite may improve the reduction of lithium ions that are transported through the solid electrolyte during cycling to lithium metal.

Therefore, the usable contact area is increased. At 71 °C, an effective conductivity of $6.1 \times 10^{-6}\text{ S cm}^{-1}$ is calculated. The activation energy does not vary significantly, when applying a graphite interface ($E_A = 0.47\text{ eV}$) compared with the reference sample in the as-deposited state ($E_A = 0.50\text{ eV}$), as the solid electrolyte is not thermally annealed in both cases. In contrast, the interlayer enables a more constant cycling with less voltage peaks, as shown in Figure 6d. The interlayer may ensure a higher contact area and less yet smaller voids between the solid electrolyte and the lithium metal as it also has been reported in literature previously.^[56,76] The symmetric cell was cycled up to 1000 $\mu\text{A cm}^{-2}$. However, at 100 and at 800 $\mu\text{A cm}^{-2}$ voltage drops occur, possibly indicating lithium dendrite formation.

3.6. Comparison with Other Production Methods

To evaluate the beneficial characteristics of the PADM and its suitability for a future solid electrolyte production, the results are summarized and compared with other reported methods.

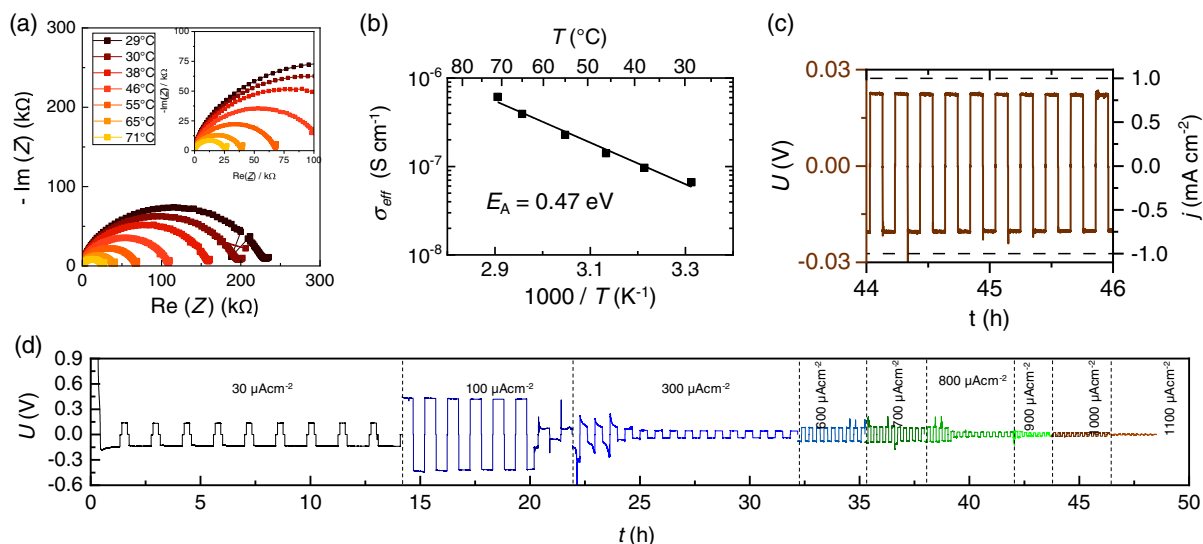


Figure 6. Electrochemical characterization of polished ALLZTO films with a graphite interlayer (type III): a) Nyquist plots of temperature-dependent EIS measurements, b) Arrhenius plot of the calculated conductivities, c) partially extracted current–voltage relationship during cycling at $1000 \mu\text{A cm}^{-2}$ from (d), d) complete cycling test at 70°C with a critical current density of $1000 \mu\text{A cm}^{-2}$.

Table 1. Overview of the electrochemical measurement data.

Sample	$\sigma_{\text{eff}} [\text{S cm}^{-1}]$		Activation energy E_A [eV]	Maximum applied current density at 70°C [$\mu\text{A cm}^{-2}$]	Cycling duration at 70°C [h]
	$T = \text{RT}$	$T = 70^\circ\text{C}$			
As-deposited	1.6×10^{-8}	2.8×10^{-7}	0.50	670	178
After thermal annealing	4.7×10^{-5}	3.1×10^{-4}	0.38	300	29
With graphite interlayer	6.6×10^{-8}	6.1×10^{-6}	0.47	1000	46

Table 1 shows the electrochemical cycling results of ALLZTO films fabricated by PAD, as presented in this work. The absolute critical current density and the cycling duration of more than 180 h of the film in the as-deposited state as well as the film conductivity after annealing at 400°C are the highest reported values for garnet-type solid electrolytes fabricated via PAD.

In addition to the sufficient effective conductivity of $4.6 \times 10^{-5} \text{ S cm}^{-1}$ at room temperature in the half-cell setup with a lithium metal electrode, the major advantage of PAD is the high deposition rate r of $0.12 \text{ mm}^3 \text{ min}^{-1}$ and therefore its industrial relevance. An additional graphite interlayer does not significantly increase the half-cell performance. In **Figure 7a,b**, the results of the annealed sample are compared with other reported fabrication methods of doped LLZO electrolytes with regard to the temperature of production or postdeposition annealing. In **Figure 8a,b**, the effective conductivity and the activation energy of those samples are compared with respect to their thickness. A complete list of all data can be found in Table S1, Supporting Information. The production of garnet-based solid electrolytes with a maximum conductivity close to $10^{-3} \text{ S cm}^{-1}$ requires high process temperatures ($>1000^\circ\text{C}$) to form dense membranes and has yet only been accomplished by tape-casted films and bulk samples that were synthesized by a solid-state or a sol–gel reaction. In addition, these electrolytes also show a minimum activation energy that is mainly dominated by

micrometer-sized grains with an ordered lattice structure. Furthermore, due to different doping strategies, the measured electrolyte conductivity varies between around 10^{-5} and $10^{-3} \text{ S cm}^{-1}$ for sintered samples. Also, the conductivity variation within other methods may be explained this way. Production methods like PLD, RF sputtering, and the here-shown PAD lead to lower conductivities and higher activation energies. These coating methods, in contrast, reduce the fabrication temperature significantly, which is highly favorable for an industrial upscaling. Furthermore, they form a direct contact to the electrode in one single process step. Considering that coating temperatures between 500 and 600°C will lead to insulating layers at cathode interfaces with a spinel structure,^[77,78] films sprayed by the PADM and annealed at 400°C for 1 h show the highest reported ionic conductivity. Although the activation energy is dominated by the grain boundaries due to the nanometer-sized grains, it agrees well with data for sintered bulk samples.

Figure 8 shows production techniques for LLZO film (or plate) fabrication in a range from 20 to 5 mm with respect to the conductivity and the activation energy. The production of bulk samples by solid-state reaction at high temperatures, as it is often reported in literature, usually takes >10 h and results in high sample thicknesses, typically larger than 1 mm. Tape casting allows a significant reduction of the film thickness

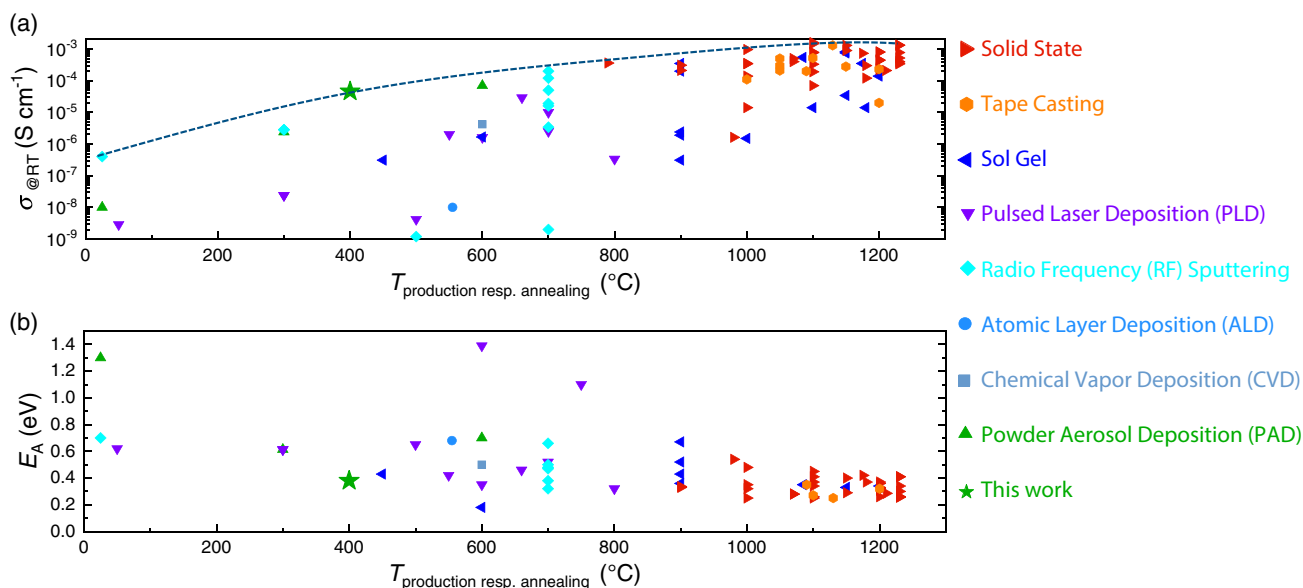


Figure 7. Comparison of conductivity and activation energy of samples obtained by different production methods (solid state,^[7,70,89–120] tape casting,^[15–19,21,23–26] sol-gel,^[93,121–134] PLD,^[30,31,33–36,38,44] RF sputtering,^[39,40,43–45,135] ALD,^[46] chemical vapor deposition (CVD),^[28,29] and PAD^[62,73,136]) for the (doped) LLZO solid electrolyte depending on the production resp. annealing temperature. The data of the annealed sample of this work are marked by an asterisk. The dotted line shows the maximum conductivity as a guide for the eye. All data points and references are also listed in Table S1, Supporting Information.

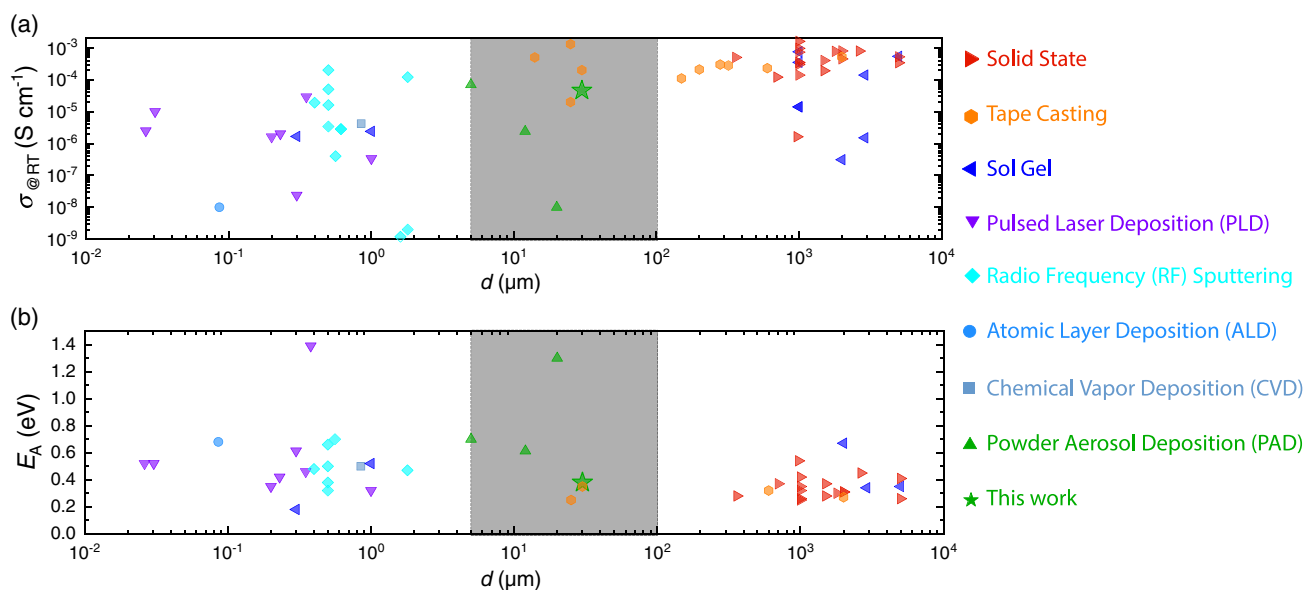


Figure 8. Comparison of the conductivity and activation energy of different production methods (solid state,^[7,70,89–120] tape casting,^[15–19,21,23–26] sol-gel,^[93,121–134] PLD,^[30,31,33–36,38,44] RF sputtering,^[39,40,43–45,135] ALD,^[46] CVD,^[28,29] and PAD^[62,73,136]) for the (doped) LLZO solid electrolyte depending on the solid electrolyte thickness. The data of the annealed sample of this work are marked by an asterisk. The target film thickness of 5–100 μm is marked in gray. All data points are also listed in Table S1, Supporting Information.

(100 μm –1 mm) at high film conductivities ($\approx 10^{-4} \text{ S cm}^{-1}$) when sintered at high temperatures above 1000 $^{\circ}\text{C}$. On one hand, the ionic conductivity of PAD films after thermal annealing is reduced by a factor of two compared with sintered tape-casted films, on the other hand, the PADM can produce films with a thickness of 1–30 μm . Therefore, the overall resistance caused

by the electrolyte is the same. For thin-film production, PLD and RF sputtering techniques are promising due to low film thicknesses (20 nm–1 μm) and high conductivity values. However, the short circuits caused by coating defects may occur significantly more often. With all production techniques, films can be fabricated with an activation energy of 0.3–0.4 eV.

Table 2. Overview of the deposition rates of different coating methods.^[28,137]

Fabrication method	Deposition rate
PLD	0.1–1 $\mu\text{m h}^{-1}$
RF sputtering	<180 nm min^{-1} resp. <10.8 $\mu\text{m h}^{-1}$
CVD	20 $\mu\text{m h}^{-1}$
PAD ^{a)}	120 $\mu\text{m min}^{-1}$

^{a)}The deposition rate for PAD is based on a coating area of $1 \times 1 \text{ mm}^2$.

Although high conductivity in conjunction with a low film thickness are the most important aspects for cell performance, additional parameters may affect the choice of the production method.^[79,80] Additional to the process temperature that has a high impact on the chemical stability of a cathode–electrolyte–composite, the required process infrastructure and process time are key factors for industrial application. For tape casting, an exact temperature control during sintering (at high temperatures) and long dwell times are necessary. Therefore, very expensive furnaces are necessary. Compared with PAD, also a subsequent fabrication process is necessary, in which the solid electrolyte is connected with the cathode. PLD and RF sputtering both are batch processes and require a very high surface quality of the substrate. Furthermore, the deposition rates are significantly lower compared with the PAD process, as shown in **Table 2**.

For the PAD process, already high coating areas are reported when using nozzle widths of up to 40 cm.^[48,81] To further increase the deposition area also a reel-to-reel setup can be installed within the deposition chamber.^[82]

4. Conclusion

The production of solid ceramic electrolytes on an industrial scale for lithium metal batteries is challenging since apart from the electrolyte thickness and its conductivity further aspects like process rate and required production temperature have to be considered. PAD is a new method to produce dense ceramic electrolytes of doped $\text{Li}_7\text{La}_3\text{Zr}_2\text{O}_{12}$ in the thickness range of 1–30 μm at room temperature with excellent bonding to the substrate.

In this work, we investigated an industrial scalable deposition setup in inert atmosphere for moisture-sensitive $\text{Al}_{0.2}\text{Li}_{6.025}\text{La}_3\text{Zr}_{1.625}\text{Ta}_{0.375}\text{O}_{12}$ powder via PAD. The modified PAD apparatus enables to homogeneously coat 30 μm -thick nanocrystalline films. Although the effective conductivity of $1.6 \times 10^{-8} \text{ S cm}^{-1}$ in a half-cell with a lithium metal electrode in the as-deposited state is below-reported values for sintered bulk samples (10^{-4} – $10^{-3} \text{ S cm}^{-1}$), a thermal post-treatment in nitrogen atmosphere at 400 °C for 1 h significantly increases the film conductivity to $4.6 \times 10^{-5} \text{ S cm}^{-1}$. Current densities higher than 500 $\mu\text{A cm}^{-2}$ at 70 °C are applied on the film in the as-deposited state. The maximum current density of the thermally annealed film is reduced, presumably due to cracks caused by different expansion coefficients of the substrate and the PAD film. A graphite interlayer between the solid electrolyte and the

lithium metal electrode on the other hand has no significant influence on the effective conductivity. Although current densities $>1 \text{ mA cm}^{-2}$ are applied on the half-cell, respectively, symmetrical cell with a graphite interlayer, the voltage curve indicates a dendrite formation at lower current densities. Nevertheless, TRL 4 for the industrial production of moisture-sensitive solid electrolytes via PAD was demonstrated by this publication. Due to the high deposition rate of 120 $\mu\text{m mm}^2 \text{ min}^{-1}$ in combination with a sufficient effective conductivity after an annealing at a relatively low temperature and low process engineering effort as well as low process invest costs, the PAD is an interesting alternative to conventional ceramic film production via tape casting. In addition, the reduced solid electrolyte film conductivity of $4.7 \times 10^{-5} \text{ S cm}^{-1}$ can be balanced by a low and adjustable film thickness. We also like to point out that the necessary post-treatment might be accomplished by laser radiation that provides a very local temperature increase exclusively within the PAD film with processing times of a few minutes without heating the entire substrate.^[83] Therefore, also conventional cathode materials like $\text{Ni}_{0.6}\text{Mn}_{0.2}\text{Co}_{0.2}\text{O}_2$ and composite cathodes with high-voltage spinel active materials or different cathode active materials that were produced via PAD^[84–88] can be coated with ALLZTO and can be subsequently thermally annealed. This can be a suitable path to produce future high-voltage lithium batteries with a ceramic electrolyte and a lithium metal anode via PAD on an industrial scale.

Supporting Information

Supporting Information is available from the Wiley Online Library or from the author.

Acknowledgements

Funding from the Federal Ministry of Education and Research of Germany (Bundesministerium für Bildung und Forschung) in the research project “ARTEMYS” (grant no. 03XP0114K) and from the Bavarian Center for Battery Technology (BayBatt) are gratefully acknowledged. The authors are indebted to Mrs. Angelika Mergner and the Bavarian Polymer Institute (BPI) for SEM imaging, as well as to the Department of Metals and Alloys (Prof. Uwe Glatzel) for XRD measurements and Mrs. Gabriele Jena from the Chair of Applied Mechanics and Fluid Dynamics for the particle size measurement.

Open access funding enabled and organized by Projekt DEAL.

Conflict of Interest

The authors declare no conflict of interest.

Data Availability Statement

Research data are not shared.

Keywords

cycle stabilities, industrial applications, lithium metal electrodes, $\text{Li}_7\text{La}_3\text{Zr}_2\text{O}_{12}$, powder aerosol deposition method

Received: March 20, 2021
Revised: April 23, 2021
Published online: May 24, 2021

- [1] J. Janek, W. G. Zeier, *Nat. Energy* **2016**, 1, 16141.
- [2] A. Manthiram, X. Yu, S. Wang, *Nat. Rev. Mater* **2017**, 2, 16103.
- [3] S. Randau, D. A. Weber, O. Kötz, R. Koerver, P. Braun, A. Weber, E. Ivers-Tiffée, T. Adermann, J. Kulisch, W. G. Zeier, F. H. Richter, J. Janek, *Nat. Energy* **2020**, 5, 259.
- [4] W. Zhao, J. Yi, P. He, H. Zhou, *Electrochem. Energ. Rev.* **2019**, 2, 574.
- [5] C. Wang, K. Fu, S. P. Kammampata, D. W. McOwen, A. J. Samson, L. Zhang, G. T. Hitz, A. M. Nolan, E. D. Wachsman, Y. Mo, V. Thangadurai, L. Hu, *Chem. Rev.* **2020**, 120, 4257.
- [6] Q. Liu, Z. Geng, C. Han, Y. Fu, S. Li, Y. He, F. Kang, B. Li, *J. Power Sources* **2018**, 389, 120.
- [7] Y. Matsuda, K. Sakamoto, M. Matsui, O. Yamamoto, Y. Takeda, N. Imanishi, *Solid State Ionics* **2015**, 277, 23.
- [8] S. Mukhopadhyay, T. Thompson, J. Sakamoto, A. Huq, J. Wolfenstine, J. L. Allen, N. Bernstein, D. A. Stewart, M. D. Johannes, *Chem. Mater.* **2015**, 27, 3658.
- [9] X. Shen, Q. Zhang, T. Ning, T. Liu, Y. Luo, X. He, Z. Luo, A. Lu, *Mater. Today Chem.* **2020**, 18, 100368.
- [10] T. Krauskopf, B. Mogwitz, H. Hartmann, D. K. Singh, W. G. Zeier, J. Janek, *Adv. Energy Mater.* **2020**, 10, 2000945.
- [11] N. J. Taylor, S. Stangeland-Molo, C. G. Haslam, A. Sharafi, T. Thompson, M. Wang, R. Garcia-Mendez, J. Sakamoto, *J. Power Sources* **2018**, 396, 314.
- [12] T. Placke, R. Kloepsch, S. Dühnen, M. Winter, *J. Solid State Electrochem.* **2017**, 21, 1939.
- [13] B. D. McCloskey, *J. Phys. Chem. Lett.* **2015**, 6, 4581.
- [14] R. Djenadic, M. Botros, C. Benel, O. Clemens, S. Indris, A. Choudhary, T. Bergfeldt, H. Hahn, *Solid State Ionics* **2014**, 263, 49.
- [15] Z. Fu, L. Zhang, J. E. Gritton, G. Godbey, T. Hamann, Y. Gong, D. McOwen, E. Wachsman, *ACS Appl. Mater. Interfaces* **2020**, 12, 24693.
- [16] K. Gao, M. He, Y. Li, Y. Zhang, J. Gao, X. Li, Z. Cui, Z. Zhan, T. Zhang, *J. Alloys Compd.* **2019**, 791, 923.
- [17] E. Hanc, W. Zając, L. Lu, B. Yan, M. Kotobuki, M. Ziąbka, J. Molenda, *J. Solid State Chem.* **2017**, 248, 51.
- [18] G. T. Hitz, D. W. McOwen, L. Zhang, Z. Ma, Z. Fu, Y. Wen, Y. Gong, J. Dai, T. R. Hamann, L. Hu, E. D. Wachsman, *Mater. Today* **2018**, 22, 50.
- [19] Z. Jiang, S. Wang, X. Chen, W. Yang, X. Yao, X. Hu, Q. Han, H. Wang, *Adv. Mater.* **2020**, 32, 1906221.
- [20] F. Chen, S. Cao, X. Xiang, D. Yang, W. Zha, J. Li, Q. Shen, L. Zhang, in *Proc. of the 42nd Int. Conf. on Advanced Ceramics and Composites: Ceramic Engineering and Science Proc.* (Eds: J. Salem, D. Koch, P. Mechnich, M. Kusnezoff, N. Bansal, J. LaSalvia, P. Balaya, Z. Fu, T. Ohji), Vol. 39, The American Ceramic Society, Westerville, OH, **2019**.
- [21] R. A. Jonson, P. J. McGinn, *Solid State Ionics* **2018**, 323, 49.
- [22] K. Liu, C.-A. Wang, *Electrochem. Commun.* **2014**, 48, 147.
- [23] R.-H. Shin, S. Son, S.-S. Ryu, H.-T. Kim, Y.-S. Han, *J. Korean Powder Metall. Inst.* **2016**, 23, 379.
- [24] C. Yang, L. Zhang, B. Liu, S. Xu, T. Hamann, D. McOwen, J. Dai, W. Luo, Y. Gong, E. D. Wachsman, L. Hu, *Proc. Natl. Acad. Sci. U. S. A.* **2018**, 115, 3770.
- [25] E. Yi, W. Wang, J. Kieffer, R. M. Laine, *J. Mater. Chem. A* **2016**, 4, 12947.
- [26] E. Yi, W. Wang, J. Kieffer, R. M. Laine, *J. Power Sources* **2017**, 352, 156.
- [27] F. Aguesse, W. Manalastas, L. Buannic, J. M. Del Lopez Amo, G. Singh, A. Llordés, J. Kilner, *ACS Appl. Mater. Interfaces* **2017**, 9, 3808.
- [28] H. Katsui, T. Goto, *Thin Solid Films* **2015**, 584, 130.
- [29] C. Loho, R. Djenadic, M. Bruns, O. Clemens, H. Hahn, *J. Electrochem. Soc.* **2016**, 164, 6131.
- [30] I. Garbayo, M. Struzik, W. J. Bowman, R. Pfenninger, E. Stilp, J. L. M. Rupp, *Adv. Energy Mater.* **2018**, 8, 1702265.
- [31] S. Kim, M. Hirayama, S. Taminato, R. Kanno, *Dalton Trans.* **2013**, 42, 13112.
- [32] S. Ohta, T. Kobayashi, J. Seki, T. Asaoka, *J. Power Sources* **2012**, 202, 332.
- [33] J. S. Park, L. Cheng, V. Zorba, A. Mehta, J. Cabana, G. Chen, M. M. Doeff, T. J. Richardson, J. H. Park, J.-W. Son, W.-S. Hong, *Thin Solid Films* **2015**, 576, 55.
- [34] R. Pfenninger, M. Struzik, I. Garbayo, E. Stilp, J. L. M. Rupp, *Nat. Energy* **2019**, 4, 475.
- [35] J. Reinacher, S. Berendts, J. Janek, *Solid State Ionics* **2014**, 258, 1.
- [36] M. Rawlence, I. Garbayo, S. Buecheler, J. L. M. Rupp, *Nanoscale* **2016**, 8, 14746.
- [37] M. Saccoccio, J. Yu, Z. Lu, S. C. Kwok, J. Wang, K. K. Yeung, M. M. Yuen, F. Ciucci, *J. Power Sources* **2017**, 365, 43.
- [38] J. Tan, A. Tiwari, *ECS Solid State Lett.* **2012**, 1, 57.
- [39] D. J. Kalita, S. H. Lee, K. S. Lee, D. H. Ko, Y. S. Yoon, *Solid State Ionics* **2012**, 229, 14.
- [40] S. Lobe, C. Dellen, M. Finsterbusch, H.-G. Gehrke, D. Sebold, C.-L. Tsai, S. Uhlenbruck, O. Guillon, *J. Power Sources* **2016**, 307, 684.
- [41] S. Lobe, C. Dellen, A. Windmüller, C.-L. Tsai, F. Vondahlen, S. Uhlenbruck, O. Guillon, *Ionics* **2018**, 24, 2199.
- [42] D. Na, B. Lee, B. Yoon, I. Seo, *J. Korean Phys. Soc.* **2020**, 76, 855.
- [43] J. Nong, H. Xu, Z. Yu, G. Zhu, A. Yu, *Mater. Lett.* **2015**, 154, 167.
- [44] M. Rawlence, A. N. Filippin, A. Waeckerlin, T.-Y. Lin, E. Cuervo-Reyes, A. Remhof, C. Battaglia, J. Rupp, S. Buecheler, *ACS Appl. Mater. Interfaces* **2018**, 10, 13720.
- [45] J. Sastre, T.-Y. Lin, A. N. Filippin, A. Priebe, E. Avancini, J. Michler, A. N. Tiwari, Y. E. Romanyuk, S. Buecheler, *ACS Appl. Energy Mater.* **2019**, 2, 8511.
- [46] E. Kazyak, K.-H. Chen, K. N. Wood, A. L. Davis, T. Thompson, A. R. Bielinski, A. J. Sanchez, X. Wang, C. Wang, J. Sakamoto, N. P. Dasgupta, *Chem. Mater.* **2017**, 29, 3785.
- [47] H. Palneedi, I. Choi, G.-Y. Kim, V. Annapureddy, D. Maurya, S. Priya, J.-W. Kim, K. J. Lee, S.-Y. Choi, S.-Y. Chung, S. J. L. Kang, J. Ryu, *J. Am. Ceram. Soc.* **2016**, 99, 2680.
- [48] J.-J. Choi, D.-S. Park, B.-G. Seong, H.-Y. Bae, *Int. J. Hydrog. Energy* **2012**, 37, 9809.
- [49] J. C. Mankins, *Acta Astronautica* **2009**, 65, 1216.
- [50] A. Banerjee, X. Wang, C. Fang, E. A. Wu, Y. S. Meng, *Chem. Rev.* **2020**, 120, 6878.
- [51] T. Krauskopf, H. Hartmann, W. G. Zeier, J. Janek, *ACS Appl. Mater. Interfaces* **2019**, 11, 14463.
- [52] A. Sharafi, E. Kazyak, A. L. Davis, S. Yu, T. Thompson, D. J. Siegel, N. P. Dasgupta, J. Sakamoto, *Chem. Mater.* **2017**, 29, 7961.
- [53] H. Yamada, T. Ito, S. P. Kammampata, V. Thangadurai, *ACS Appl. Mater. Interfaces* **2020**, 12, 36119.
- [54] K. K. Fu, Y. Gong, B. Liu, Y. Zhu, S. Xu, Y. Yao, W. Luo, C. Wang, S. D. Lacey, J. Dai, Y. Chen, Y. Mo, E. Wachsman, L. Hu, *Sci. Adv.* **2017**, 3, 1601659.
- [55] X. Han, Y. Gong, K. K. Fu, X. He, G. T. Hitz, J. Dai, A. Pearse, B. Liu, H. Wang, G. Rubloff, Y. Mo, V. Thangadurai, E. D. Wachsman, L. Hu, *Nat. Mater.* **2017**, 16, 572.
- [56] Y. Shao, H. Wang, Z. Gong, D. Wang, B. Zheng, J. Zhu, Y. Lu, Y.-S. Hu, X. Guo, H. Li, X. Huang, Y. Yang, C.-W. Nan, L. Chen, *ACS Energy Lett.* **2018**, 3, 1212.
- [57] S. Adams, R. P. Rao, *J. Mater. Chem.* **2012**, 22, 1426.
- [58] E. Rangasamy, J. Wolfenstine, J. Sakamoto, *Solid State Ionics* **2012**, 206, 28.

- [59] D. Hanft, J. Exner, M. Schubert, T. Stöcker, P. Fuierer, R. Moos, *J. Ceram. Sci. Technol.* **2017**, *6*, 147.
- [60] J. Akedo, *J. Therm. Spray. Tech.* **2008**, *17*, 181.
- [61] J. Akedo, *J. Am. Ceram. Soc.* **2006**, *89*, 1834.
- [62] D. Hanft, J. Exner, R. Moos, *J. Power Sources* **2017**, *361*, 61.
- [63] Y. Zhu, J. G. Connell, S. Tepavcevic, P. Zapol, R. Garcia-Mendez, N. J. Taylor, J. Sakamoto, B. J. Ingram, L. A. Curtiss, J. W. Freeland, D. D. Fong, N. M. Markovic, *Adv. Energy Mater.* **2019**, *9*, 1803440.
- [64] E. Ivers-Tiffée, W. von Münch, in *Werkstoffe der Elektrotechnik. Mit 40 Tabellen*, Teubner, Wiesbaden **2007**, pp. 57, 67, 68.
- [65] C. H. Hamann, W. Vielstich, in *Elektrochemie*, Wiley-VCH-Verlag GmbJ & Co. KGaA, Weinheim **2005**, pp. 203–205.
- [66] D. Hanft, in *Aerosolbasierte Kaltabscheidung Lithium-Ionen leitender Festelektrolytschichten mit Granatstruktur*, Shaker, Düren **2019**, pp. 67–74.
- [67] L. Cheng, E. J. Crumlin, W. Chen, R. Qiao, H. Hou, S. Franz Lux, V. Zorba, R. Russo, R. Kosteci, Z. Liu, K. Persson, W. Yang, J. Cabana, T. Richardson, G. Chen, M. Doeff, *Phys. Chem. Chem. Phys.* **2014**, *16*, 18294.
- [68] J. Exner, T. Nazarenus, D. Hanft, J. Kita, R. Moos, *Adv. Mater.* **2020**, *32*, 1908104.
- [69] M. Schubert, J. Exner, R. Moos, *Materials* **2014**, *7*, 5633.
- [70] R. Murugan, V. Thangadurai, W. Weppner, *Angew. Chem., Int. Ed.* **2007**, *46*, 7778.
- [71] J. Exner, J. Kita, R. Moos, *J. Mater. Sci.* **2019**, *54*, 13619.
- [72] D.-W. Lee, H.-J. Kim, Y.-H. Kim, Y.-H. Yun, S.-M. Nam, *J. Am. Ceram. Soc.* **2011**, *94*, 3131.
- [73] C.-W. Ahn, J.-J. Choi, J. Ryu, B.-D. Hahn, J.-W. Kim, W.-H. Yoon, J.-H. Choi, D.-S. Park, *J. Electrochem. Soc.* **2015**, *162*, A60.
- [74] M. Hahn, D. Rosenbach, A. Krimalowski, T. Nazarenus, R. Moos, M. Thelakkat, M. A. Danzer, *Electrochim. Acta* **2020**, *344*, 136060.
- [75] A. J. Samson, K. Hofstetter, S. Bag, V. Thangadurai, *Energy Environ. Sci.* **2019**, *12*, 2957.
- [76] G. V. Alexander, M. S. Indu, S. Kamakshy, R. Murugan, *Electrochim. Acta* **2020**, *332*, 135511.
- [77] Y. Ren, T. Liu, Y. Shen, Y. Lin, C.-W. Nan, *J. Materiomics* **2016**, *2*, 256.
- [78] L. Miara, A. Windmüller, C.-L. Tsai, W. D. Richards, Q. Ma, S. Uhlenbruck, O. Guillon, G. Ceder, *ACS Appl. Mater. Interfaces* **2016**, *8*, 26842.
- [79] J. Schnell, H. Knörzer, A. J. Imbsweiler, G. Reinhart, *Energy Technol.* **2020**, *8*, 1901237.
- [80] J. Schnell, F. Tietz, C. Singer, A. Hofer, N. Billot, G. Reinhart, *Energy Environ. Sci.* **2019**, *12*, 1818.
- [81] S. Kirihara, K. Nakata, in *Multi-dimensional Additive Manufacturing*, Springer Singapore, Singapore **2021**, pp. 107–127.
- [82] T. Arndt, US 2013/0123112 A1, **2011**.
- [83] T. Nazarenus, J. Kita, R. Moos, J. Exner, *Adv. Mater. Interfaces* **2020**, *7*, 2001114.
- [84] R. Inada, K. Okuno, S. Kito, T. Tojo, Y. Sakurai, *Materials* **2018**, *11*, 1570.
- [85] Y. Iriyama, M. Wadaguchi, K. Yoshida, Y. Yamamoto, M. Motoyama, T. Yamamoto, *J. Power Sources* **2018**, *385*, 55.
- [86] S. Iwasaki, T. Hamanaka, T. Yamakawa, W. C. West, K. Yamamoto, M. Motoyama, T. Hirayama, Y. Iriyama, *J. Power Sources* **2014**, *272*, 1086.
- [87] T. Kato, S. Iwasaki, Y. Ishii, M. Motoyama, W. C. West, Y. Yamamoto, Y. Iriyama, *J. Power Sources* **2016**, *303*, 65.
- [88] I. Kim, J. Park, T.-H. Nam, K.-W. Kim, J.-H. Ahn, D.-S. Park, C.-W. Ahn, G. Wang, H.-J. Ahn, *J. Power Sources* **2013**, *244*, 646.
- [89] J. van den Broek, S. Afyon, J. L. M. Rupp, *Adv. Energy Mater.* **2016**, *6*, 1600736.
- [90] R. Inada, S. Yasuda, H. Hosokawa, M. Saito, T. Tojo, Y. Sakurai, *Batteries* **2018**, *4*, 26.
- [91] D. O. Shin, K. Oh, K. M. Kim, K.-Y. Park, B. Lee, Y.-G. Lee, K. Kang, *Sci. Rep.* **2015**, *5*, 18053.
- [92] Y. Zhang, F. Chen, R. Tu, Q. Shen, X. Zhang, L. Zhang, *Solid State Ionics* **2016**, *284*, 53.
- [93] Y. Shimonishi, A. Toda, T. Zhang, A. Hirano, N. Imanishi, O. Yamamoto, Y. Takeda, *Solid State Ionics* **2011**, *183*, 48.
- [94] M. Kotobuki, K. Kanamura, Y. Sato, T. Yoshida, *J. Power Sources* **2011**, *196*, 7750.
- [95] Z. Hu, H. Liu, H. Ruan, R. Hu, Y. Su, L. Zhang, *Ceram. Int.* **2016**, *42*, 12156.
- [96] R.-J. Chen, M. Huang, W.-Z. Huang, Y. Shen, Y.-H. Lin, C.-W. Nan, *Solid State Ionics* **2014**, *265*, 7.
- [97] R. Sudo, Y. Nakata, K. Ishiguro, M. Matsui, A. Hirano, Y. Takeda, O. Yamamoto, N. Imanishi, *Solid State Ionics* **2014**, *262*, 151.
- [98] C.-L. Tsai, E. Dashjav, E.-M. Hammer, M. Finsterbusch, F. Tietz, S. Uhlenbruck, H. P. Buchkremer, *J. Electroceram.* **2015**, *35*, 25.
- [99] H. Buschmann, J. Dölle, S. Berendts, A. Kuhn, P. Bottke, M. Wilkening, P. Heitjans, A. Senyshyn, H. Ehrenberg, A. Lotnyk, V. Duppel, L. Kienlee, J. Janek, *Phys. Chem. Chem. Phys.* **2011**, *13*, 19378.
- [100] M. Huang, T. Liu, Y. Deng, H. Geng, Y. Shen, Y. Lin, C.-W. Nan, *Solid State Ionics* **2011**, *204–205*, 41.
- [101] W. Xia, B. Xu, H. Duan, Y. Guo, H. Kang, H. Li, H. Liu, *ACS Appl. Mater. Interfaces* **2016**, *8*, 5335.
- [102] E. Rangasamy, J. Wolfenstine, J. Allen, J. Sakamoto, *J. Power Sources* **2013**, *230*, 261.
- [103] J. Wolfenstine, J. Ratchford, E. Rangasamy, J. Sakamoto, J. L. Allen, *Mater. Chem. Phys.* **2012**, *134*, 571.
- [104] Y. Matsuda, A. Sakaida, K. Sugimoto, D. Mori, Y. Takeda, O. Yamamoto, N. Imanishi, *Solid State Ionics* **2017**, *311*, 69.
- [105] D. Rettenwander, G. Redhammer, F. Preishuber-Pflügl, L. Cheng, L. Miara, R. Wagner, A. Welzl, E. Suard, M. M. Doeff, M. Wilkening, J. Fleig, G. Amthauer, *Chem. Mater.* **2016**, *28*, 2384.
- [106] S. Ohta, T. Kobayashi, T. Asaoka, *J. Power Sources* **2011**, *196*, 3342.
- [107] J. Awaka, N. Kijima, H. Hayakawa, J. Akimoto, *J. Solid State Chem.* **2009**, *182*, 2046.
- [108] S. Ramakumar, L. Satyanarayana, S. V. Manorama, R. Murugan, *Phys. Chem. Chem. Phys.* **2013**, *15*, 11327.
- [109] A. Dumon, M. Huang, Y. Shen, C.-W. Nan, *Solid State Ionics* **2013**, *243*, 36.
- [110] L. Cheng, J. S. Park, H. Hou, V. Zorba, G. Chen, T. Richardson, J. Cabana, R. Russo, M. Doeff, *J. Mater. Chem. A* **2014**, *2*, 172.
- [111] H. Buschmann, S. Berendts, B. Mogwitz, J. Janek, *J. Power Sources* **2012**, *206*, 236.
- [112] Y. Cao, Y.-Q. Li, X.-X. Guo, *Chinese Phys. B* **2013**, *22*, 78201.
- [113] C. Deviannapoorani, L. Dhivya, S. Ramakumar, R. Murugan, *J. Power Sources* **2013**, *240*, 18.
- [114] R. Murugan, S. Ramakumar, N. Janani, *Electrochem. Commun.* **2011**, *13*, 1373.
- [115] C. Deviannapoorani, S. Ramakumar, N. Janani, R. Murugan, *Solid State Ionics* **2015**, *283*, 123.
- [116] J.-F. Wu, E.-Y. Chen, Y. Yu, L. Liu, Y. Wu, W. K. Pang, V. K. Peterson, X. Guo, *ACS Appl. Mater. Interfaces* **2017**, *9*, 1542.
- [117] Y.-T. Chen, A. Jena, W. K. Pang, V. K. Peterson, H.-S. Sheu, H. Chang, R.-S. Liu, *J. Phys. Chem. C* **2017**, *121*, 15565.
- [118] W. Xue, Y. Yang, Q. Yang, Y. Liu, L. Wang, C. Chen, R. Cheng, *RSC Adv.* **2018**, *8*, 13083.
- [119] S. Ohta, J. Seki, Y. Yagi, Y. Kihira, T. Tani, T. Asaoka, *J. Power Sources* **2014**, *265*, 40.
- [120] J.-F. Wu, W. K. Pang, V. K. Peterson, L. Wei, X. Guo, *ACS Appl. Mater. Interfaces* **2017**, *9*, 12461.
- [121] M. Zarabian, M. Bartolini, P. Pereira-Almao, V. Thangadurai, *J. Electrochem. Soc.* **2017**, *164*, 1133.

- [122] K. Tadanaga, H. Egawa, A. Hayashi, M. Tatsumisago, J. Mosa, M. Aparicio, A. Duran, *J. Power Sources* **2015**, 273, 844.
- [123] R.-J. Chen, M. Huang, W.-Z. Huang, Y. Shen, Y.-H. Lin, C.-W. Nan, *J. Mater. Chem. A* **2014**, 2, 13277.
- [124] F. M. Pesci, R. H. Brugge, A. K. O. Hekselman, A. Cavallaro, R. J. Chater, A. Aguadero, *J. Mater. Chem. A* **2018**, 6, 19817.
- [125] Y. Li, J.-T. Han, C.-A. Wang, S. C. Vogel, H. Xie, M. Xu, J. B. Goodenough, *J. Power Sources* **2012**, 209, 278.
- [126] H. El Shinawi, J. Janek, *J. Power Sources* **2013**, 225, 13.
- [127] S. Toda, K. Ishiguro, Y. Shimonishi, A. Hirano, Y. Takeda, O. Yamamoto, N. Imanishi, *Solid State Ionics* **2013**, 233, 102.
- [128] I. Kokal, M. Somer, P. Notten, H. T. Hintzen, *Solid State Ionics* **2011**, 185, 42.
- [129] A. A. Raskovalov, E. A. Il'ina, B. D. Antonov, *J. Power Sources* **2013**, 238, 48.
- [130] R. Takano, K. Tadanaga, A. Hayashi, M. Tatsumisago, *Solid State Ionics* **2014**, 255, 104.
- [131] N. Rosenkiewitz, J. Schuhmacher, M. Bockmeyer, J. Deubener, *J. Power Sources* **2015**, 278, 104.
- [132] C.-H. Lee, G.-J. Park, J.-H. Choi, C.-H. Doh, D.-S. Bae, J.-S. Kim, S.-M. Lee, *Mater. Res. Bull.* **2016**, 83, 309.
- [133] R. H. Brugge, A. K. O. Hekselman, A. Cavallaro, F. M. Pesci, R. J. Chater, J. A. Kilner, A. Aguadero, *Chem. Mater.* **2018**, 30, 3704.
- [134] H. El-Shinawi, E. J. Cussen, S. A. Corr, *Dalton Trans.* **2017**, 46, 9415.
- [135] J. Sastre, A. Priebe, M. Döbeli, J. Michler, A. N. Tiwari, Y. E. Romanyuk, *Adv. Mater. Interfaces* **2020**, 7, 2000425.
- [136] R. Inada, T. Okada, A. Bando, T. Tojo, Y. Sakurai, *Prog. Nat. Sci.: Mater. Int.* **2017**, 27, 350.
- [137] A. R. Nyaiesh, L. Holland, *Pergamon Press* **1981**, 31, 315.